

# Experimental study of the effects of exhaust plume and nozzle length on transonic and supersonic axisymmetric base flows

*Paul van Gent, Qais Payanda, Steve Brust, Bas van Oudheusden and Ferry Schrijer*

*Department of Aerospace Engineering, Delft University of Technology,*

*Kluyverweg 1, 2629 HS Delft, The Netherlands*

*email: p.l.vangent@tudelft.nl*

## Abstract

PIV measurements have been carried out to study the effect of exhaust plume and nozzle length on the flow topology and mean pressure distribution of axisymmetric base flows at freestream Mach numbers 0.76 and 2.20. Four different nozzle lengths with and without exhaust plume have been tested. The use of different nozzle lengths leads to flow cases in which the shear layer impinges on the model (solid reattachment), on the flow downstream of the model (fluidic reattachment), and intermittently on the model and on the flow (hybrid reattachment). An increase in nozzle length and the presence of an exhaust plume led to an increase in mean reattachment length at Mach 2.20, whereas no significant change in reattachment length was observed at Mach 0.76. The flow cases with the longest nozzles for which solid reattachment occurred showed significantly higher turbulent kinetic energy levels, at Mach 2.20, but significantly lower levels at Mach 0.76. Comparisons of flow cases with a long nozzle without a plume and flow cases with a short nozzle but with a plume suggest that the presence of the plume cannot accurately be modelled by replacing the plume with a solid geometry. Pressure results showed that the location of the low-pressure region downstream of the base remains rather invariant for different flow cases with and without plume and for different nozzle lengths. An increase in nozzle length leads to higher local pressure at the nozzle exit and therefore results in a less under-expanded or more over-expanded plume.

## 1. Introduction

During ascent of a launch vehicle, its nozzle and other structures near the base are subject to pressure and heat loads. The relatively low pressure in the base region contributes significantly to the overall drag of the vehicle. In addition, the inherent unsteadiness of the flow gives rise to fluctuating pressure-induced side-loads on the nozzle. In particular during transonic flight, the low-frequency component of these side-loads may excite a structural response (buffeting) and cause structural failure. On top of that, the entrainment of hot exhaust gasses in the recirculation region may lead to significant heat loads. In view of the above, the quantification of pressure and heat loads is essential for the safe and efficient design of launch vehicles.

The geometry of the launcher base can be simplified to a cylindrical main body and a cylindrical afterbody that represent the main stage and nozzle, respectively. Although a number of studies investigated realistic scale models (e.g. [1]), using such a generic geometry is a more common practice in the context of academic research.

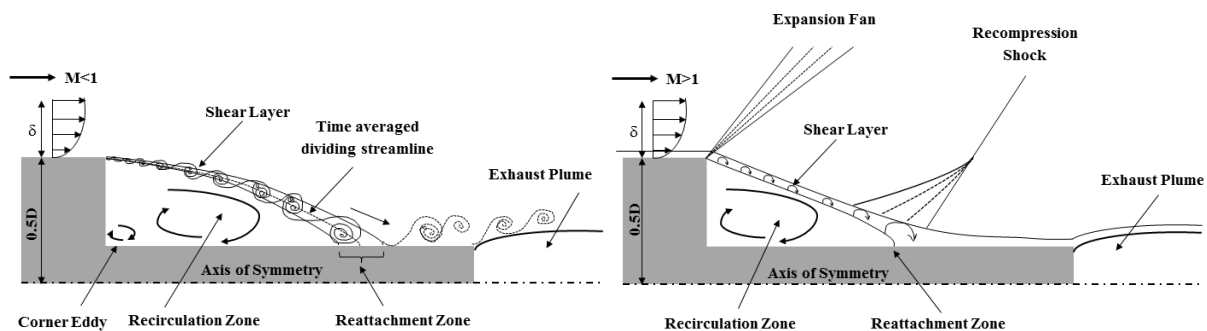


Figure 1: Schematic of flow topology, subsonic flow (left) supersonic flow (right) (adapted from [2, 3])

Figure 1 shows a side view of a generic axisymmetric base flow. Due to the abrupt change in geometry, the flow separates at the trailing edge of the main body. A recirculation region is formed that is separated from the outer flow by a shear layer. Depending on the length of the afterbody (the design of the launcher), the shear layer impinges on the afterbody (nozzle) or on the flow further downstream. A special situation exists if, in view of the unsteadiness of the flow, the reattachment intermittently occurs on the afterbody and on the flow. Deprés et al. (2004) [4] refers to these different flow configurations as solid, fluidic and hybrid reattachment. The presence of an exhaust plume exiting from the afterbody has two important effects on the flow field. Firstly, a plume causes displacement of the outer flow due to blockage. Secondly, entrainment at the plume boundary leads to acceleration of the outer flow moving downstream [5]. The blockage by the plume tends to increase the pressure felt at the base while the entrainment acts to decrease the pressure [5]. The impact of the plume is dependent on the type of reattachment and can be small if (solid) reattachment occurs on the afterbody, well upstream of the plume [4].

During ascent of the launcher vehicle the Mach number of the external flow increases, while the ambient pressure and temperature decrease. This causes the typical plume state at the nozzle exit to change from overexpanded to increasingly underexpanded. At the transition from subsonic to supersonic flight a Prandtl-Meyer expansion fan is formed at the trailing edge of the main body, while a shock wave is formed at reattachment as the flow turns back in the direction of the freestream flow (see Fig.1). Additional shock waves may be formed due to displacement of the flow by the plume. The reattachment length in supersonic flow conditions is significantly shorter than for the subsonic case. Due to the influence of a plume, however, the shear layer may become detached from the afterbody leading to a significantly larger recirculation region and an increase in base pressure [6].

The base flow has been investigated in numerous experimental and numerical assessments that aimed to uncover the driving mechanisms of the flow dynamics and quantify the associated pressure loads. The majority of studies have focussed on free stream Mach numbers around 0.7 for which the critical mechanical loads typically occur (e.g. [4, 7–10]). Others have focussed on supersonic flow conditions (e.g. [11–14]), and a small number of studies compared both flow regimes (e.g. [15–17]). In view of the importance of quantifying (fluctuating) pressure loads to assist future design activities, previous experimental assessments predominantly focussed on analysing pressure data measured at the model surface by pressure transducers. Several studies used particle image velocimetry (PIV) which allows experimental characterisation of the flow in terms of ensembles of instantaneous velocity fields. PIV has been used to investigate the unsteady behaviour of the flow [1, 9, 10, 15], to obtain high-precision measurements of the mean flow field and Reynolds stress distributions [18], and to assess the impact of control devices [19, 20]. A small number of studies used PIV in configurations with exhaust plumes [13, 16]. With a few exceptions (e.g. [21, 22]), the possibility to process PIV velocity data to reconstruct pressure fields has however been largely explored. Whereas the use of time-resolved PIV measurements allows reconstructing instantaneous pressure fields, the use of ensembles of uncorrelated PIV measurements allow reconstructing the mean pressure field [23]. The technique is particularly beneficial when the model geometry imposes spatial limitations for the installation of surface pressure tabs or sensors; as is the case for a model equipped with a nozzle to generate an exhaust plume.

In view of the above, the focus of the present study is to characterise the flow topology and pressure distribution for subsonic and supersonic axisymmetric base flows, for flow cases with and without exhaust plumes and for different nozzle lengths. Ensembles of velocity fields are obtained by planar PIV and processed to obtain the spatial distribution of mean velocity, turbulent kinetic energy and mean pressure.

## 2. Experimental arrangements and measurement techniques

### 2.1 Flow facility and model

The experiments are performed in the transonic-supersonic wind tunnel (TST-27) of the High-Speed Aerodynamics Laboratories at Delft University of Technology. The facility has a test section of dimensions 280 mm (width)  $\times$  270 mm (height). Table 1 lists the most relevant flow characteristics. The freestream conditions refer to the flow conditions over the main body of the model (see Figure 2 (left)). The freestream pressure ( $p_\infty$ ) was measured via a tap in the main body on the model located 65 mm (1.3D) upstream of the base. Other freestream flow parameters have been calculated using isentropic flow relations. The wind tunnel is operated at nominal Mach numbers of 0.70 and 2.20. Due to blockage effects, the effective freestream Mach number ( $M_\infty$ ) for the subsonic case is  $M_\infty = 0.76$ . Indicated precision ranges correspond to variations of flow parameters over a run and between different runs. From the PIV data, the thickness of the boundary layer on the model just upstream of the base is estimated to be  $\delta = 3$  mm.

The model shown in Figure 2 (left) is the same model as used within the framework of FESTIP (Future European Space Transportation Investigation Program) [24]. It has been tested extensively in a series of experimental and numerical assessments (e.g. [10, 13, 25, 26]). The model has a conical nose with a semi-apex angle of  $11^\circ$  and a nose radius of 7.5 mm. The cylindrical main body has a diameter ( $D$ ) of 50 mm. The nose and main body have a

comparable length. The afterbody contains a nozzle that allows generating an exhaust plume of dry, unheated air that is supplied through tubing in the model support. Compressed air is supplied to the model from four 50 liter tanks each filled to a pressure of 300 bar. The tanks are placed directly next to the test section.

Table 1: Flow characteristics

Parameter	Subsonic	Supersonic
Free stream Mach number ( $M_\infty$ )	$0.76 \pm 0.01$	$2.20 \pm 0.01$
Total pressure ( $p_0$ )	$1.98 \pm 0.01$ bar	$2.48 \pm 0.01$ bar
Free stream pressure ( $p_\infty$ )	$1.38 \pm 0.01$ bar	$0.23 \pm 0.01$ bar
Total temperature ( $T_0$ )	$273 \pm 3$ K	$277 \pm 3$ K
Free stream velocity ( $U_\infty$ )	$239 \pm 3$ m s <sup>-1</sup>	$534 \pm 3$ m s <sup>-1</sup>
Reynolds number ( $Re_D$ )	$1.5 \times 10^6$	$3.3 \times 10^6$
Jet Mach number at nozzle exit ( $M_{e,jet}$ )	3.5	3.5
Total jet pressure ( $p_{0,jet}$ )	$22 \text{ bar} \pm 2$	$27 \text{ bar} \pm 2$
Static jet pressure at nozzle exit ( $p_{e,jet}$ )	$0.28 \text{ bar} \pm 0.01$	$0.36 \text{ bar} \pm 0.01$
Total jet temperature ( $T_{0,jet}$ )	<288 K	<288 K
Nozzle pressure ratio ( $NPR = p_{0,jet}/p_{e,jet}$ )	76	75

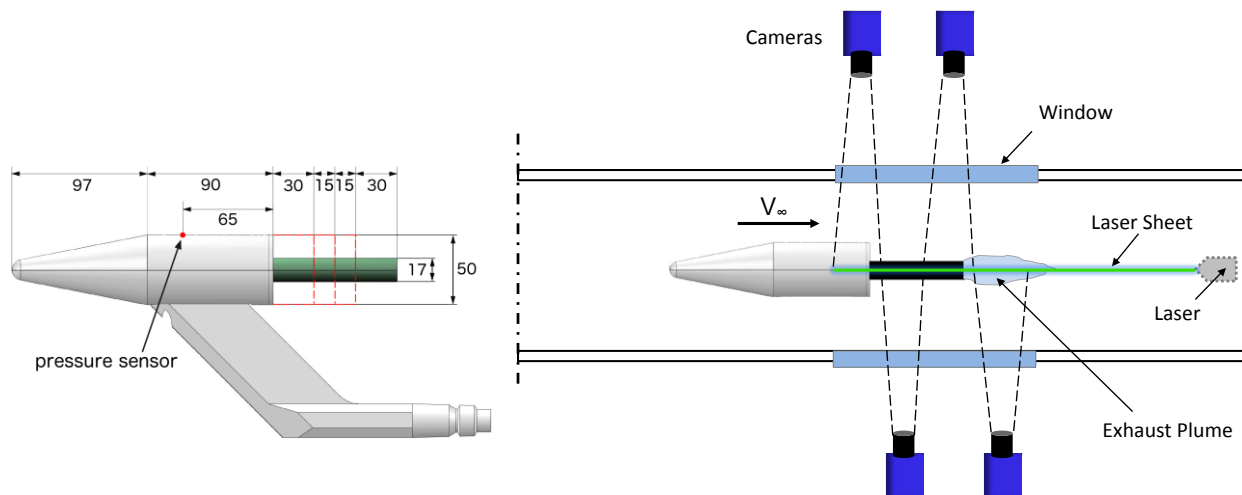


Figure 2: Schematic of the model, side view (left); and PIV setup, top view (right)

The present experiment considers four nozzle lengths:  $L/D = 1.8, 1.2, 0.9$  and  $0.6$ . For this the original model has been retrofitted by a nozzle with an adjustable length, achieved by sliding different collars over the nozzle. The model is equipped with a trip strip (0.15 mm diameter) applied at about 40% of the nose to ensure a fully developed, turbulent boundary layer. A pressure tap on top of the main body is connected to a Druck Ltd PDCR-22, 0-15 psi differential pressure transducer and used to determine the effective free stream Mach number. The geometry of the nozzle in the afterbody is conical with a divergence of  $15^\circ$  (half angle of  $7.5^\circ$ ). The area ratio between the nozzle exit and throat diameters is  $A_{exit}/A^* = 6.79$ , so that the exit Mach number is  $M_{e,jet} = 3.5$ . The design Mach number has been chosen to avoid condensation of the jet at the desired flow conditions. The total pressure of the jet has been selected so that the ratio of static pressure at the nozzle exit and static freestream pressure is similar as during the ascent of the Ariane 5 when it travels at Mach 0.7 and 2.2, respectively [27, 28]. The pressure ratio and the Mach number are the most important flow parameters to be duplicated to achieve a similar initial inclination angle of the jet which is important to achieve a similarity in the flow topology and the pressure distribution in the base region [29]. The resulting jet is over-expanded for the case of  $M_\infty = 0.76$  and under-expanded for the case  $M_\infty = 2.20$ . It is noted that the precise shape of the plume is not defined by the ratio of the static jet pressure and the pressure in the freestream, but by the ratio of the static jet pressure and local static pressure at the location of the plume. The difference between both ratios depends on the geometry of the model, in particular the nozzle length. Due to the control system of the compressed air supply, the total and static jet pressure drop up about 10% over the

duration of each run (about 30 seconds). The compressed air that is fed to the model is stored at ambient temperature of about 288 K. The total jet temperature ( $T_{0,jet}$ ) is lower due to heat losses in the piping to the model.

## 2.2 PIV measurements

PIV measurements were performed in a streamwise-oriented plane downstream of the step. The size of the measurement plane is  $2.8D \times 1.0D$  (140 mm  $\times$  50 mm,  $L \times H$ ). Figure 2 (right) provides an overview of the PIV setup. The flow in the wind tunnel was seeded with titanium dioxide ( $TiO_2$ ) particles of the type Kemira P580. The particles have a primary crystal size of 30 nm (the actual particles form agglomerates of approximately 500 nm, [30]), a nominal density of  $150 \text{ kg m}^{-3}$  and a particle response time of  $\tau_p = 2.56 \mu\text{s}$  [31]. The particles were introduced in the tunnel by a seeding rake placed in the settling chamber, which was connected to a cyclone seeding generator. At  $M_\infty = 0.76$ , the distribution of particles was relatively uniform in the field-of-view and the seeding intensity was relatively constant over different snapshots. For the case of  $M_\infty = 2.20$ , however, the seeding was intermittent and strong variations in particle image density occurred throughout the field-of-view (see also [13]). Particles were illuminated by a double-cavity Nd-Yag laser of the type Spectra-Physics Quanta Ray PIV-400. The laser light was introduced into the wind tunnel by an optical probe that was located downstream of the test section. The laser light was shaped using optics inside the probe into a sheet with a thickness of about 2 mm.

Recording was performed by four LaVision Imager LX 2MP cameras (pixel resolution  $1628 \times 1236$  pixel, pixel size  $4.4 \times 4.4 \mu\text{m}$ ) equipped with Nikon objectives of 105 mm operated at an aperture of f/8.0. The field-of-views of the different cameras were placed next to each other in streamwise direction with an overlap of about 4 mm. These arrangements resulted in a digital resolution of  $30.3 \text{ pixel mm}^{-1}$  (optical magnification 0.19) and particle image diameters of about 2.5 pixels. Recording was performed at 5 Hz in double-frame mode. The time separation between two consecutive laser pulses was set at  $2.5 \mu\text{s}$  and  $1.0 \mu\text{s}$  for  $M_\infty = 0.76$  and  $M_\infty = 2.20$ , respectively. The resulting particle displacement in the freestream was 25.6 pixels and 22.9 pixels, respectively. The synchronization of all components and the acquisition of image data were ensured by an external timing unit.

The contrast of the particle images was enhanced by subtracting the local minimum intensity in each run and the minimum intensity within 31 pixel-sized kernels. The resulting intensity was normalised by a min-max filter with a kernel of 6 pixels. Velocity vector fields were obtained using a multi-grid correlation procedure with Gaussian weighted windows. Intermediate vector fields were filtered before the next iteration by Gaussian smoothing. The final three iterations were performed with an interrogation window size of 48 pixels with a 75% overlap, resulting in a vector spacing of 0.40 mm. PIV recording and processing were performed using LaVision DaVis software, versions 8.1.2 and 8.3.1, respectively.

The recorded images from the four cameras were analysed separately. The resulting vector fields were stitched to each other and transferred to a common grid by linear interpolation. The final grid consists of  $420 \times 137$  ( $L \times H$ ) points with a similar spacing as in the original vector fields. 500 snapshots were obtained in four runs of 125 snapshots for each of the 16 cases considered (4 nozzle lengths; 2 Mach numbers; with and without jet). Based on visual inspection of the recorded images and final vector fields, 5 - 15% of the snapshots were deemed to suffer from insufficient seeding quality, depending on the case considered. These snapshots were removed before performing any subsequent analysis.

The accuracy of the PIV measurement depends on how well the tracer particles follow the flow and how accurately the displacement of the particles can be determined from camera recordings. A detailed analysis of the measurement uncertainty is beyond the scope of this paper. An indicative estimate of the uncertainty in mean velocity and turbulent kinetic energy (TKE) is obtained by assuming that the errors are random and have a Gaussian distribution. Under those assumptions and based on the ensemble size ( $N$ ) of 500 images, the statistical convergence uncertainty in mean velocity is estimated to be  $N^{-1/2} = 4.5\%$  of the standard deviation of the measured velocity fluctuations which translates to a maximum of about 1%  $U_\infty$ . The uncertainty in TKE is estimated to be smaller than 6.3%, according to  $U_{TKE} = ((\langle u'^2 \rangle + \langle v'^2 \rangle) / (2N))^{1/2} < (\langle u' \rangle + \langle v' \rangle) / (2N)^{1/2} = TKE (2/N)^{1/2} = 6.3\% TKE$ .

## 2.3 Mean pressure field reconstruction from PIV measurements

The background and working principle for the procedure for obtaining pressure from velocity fields for compressible flows is outlined in [22, 32, 33]. Starting from the momentum equation, the mean pressure gradient can be written as follows (see equation 1).

$$\frac{\partial \ln(\langle p \rangle / p_\infty)}{\partial x_i} = -\frac{1}{RT} \left( \langle u_j \rangle \frac{\partial \langle u_j \rangle}{\partial x_j} + \frac{\partial \langle u_i u_j \rangle}{\partial x_j} \right) \quad (1)$$

where  $p$  is the pressure,  $R$  is the specific gas constant,  $T$  is the temperature and  $u_i$  denotes the velocity in direction  $x_i$ . The density has been eliminated from the original momentum equation with the gas law, while the temperature in equation (1) is related to the freestream quantities and local velocity magnitude by assuming the flow to be adiabatic:

$$T = \frac{U_\infty^2 + \frac{\gamma-1}{2} M_\infty^2 (U_\infty^2 - \langle V \rangle^2)}{\gamma R M_\infty^2} \quad (2)$$

Here  $\gamma$  is the ratio of specific heats and  $V$  is the velocity magnitude. Note that equation (1) does not contain any temporal derivatives since these dropped out in the derivation when taking the average in time. The viscous term has been discarded as several studies showed that its contribution is negligible for flows with high Reynolds numbers (e.g., [22, 33]). The equation does not consider the spatial gradient of the mean density and the effect of density fluctuations [32], as a preliminary investigation showed that inclusion of the associated terms does not lead to more accurate results. Equation (1) was solved for pressure using a similar discretisation as proposed by [34]. The resulting linear system of equations was solved using the Matlab algorithm *mldivide*. Pressure gradients were used implicitly as Neumann boundary conditions on all sides of the domain except for the top of the domain for  $-0.1 < x/D < 0.5$ . Here the logarithm of the pressure ratio obtained from isentropic flow relations was prescribed. The validity of assuming isentropic flow at distances larger than two step-heights from the afterbody was demonstrated in [22]. The validity of the pressure reconstruction was checked by comparing PIV-based pressure values to reference pressure measurements in a model with pressure sensors.

### 3. Results

#### 3.1 Mean velocity

Figure 3 and Figure 4 show the mean flow organisation for  $M_\infty = 0.76$  and  $M_\infty = 2.20$ , respectively. Colours indicate the value of mean streamwise velocity. Black contour lines indicates zero streamwise velocity. Left figures correspond to the cases without plume and right figures to the cases with a plume. The nozzle length increases from top to bottom from  $L/D = 0.6$  to  $0.9$ ,  $1.2$  and  $1.8$ . The origin is located at the streamwise location of trailing edge of the main body ( $x/D = 0$ ) and at the centre line of the afterbody ( $y/D = 0$ ). Bright grey indicates the location of the model. Dark grey indicates the shape of the plume which was estimated as the region where no velocity measurements could be obtained in at least 20% of the instantaneous velocity fields due to a lack of seeding particles. Differences in the shape of the plume for different flow cases will be discussed in section 3.3. To facilitate comparison of the different cases, Table 2 lists the mean reattachment length and the absolute value of the maximum mean backflow velocity. The mean reattachment length was inferred from the figures by taking the streamwise location where the zero streamwise velocity contour (black line) intersects the geometry or the plume.

Figure 3 and Figure 4 show a uniform incoming flow that deflects towards the afterbody as the flow moves over the step. Additional analysis showed that the inflow velocity varies no more than  $0.01U_\infty$  between cases with and without plume and by no more than  $0.02U_\infty$  between cases with different nozzle lengths. The flow separates as it passes over the step leading to a large-scale recirculation region with significant back flow (see table 4). The outer flow and recirculation region are separated by a shear layer. In absence of an exhaust plume, another larger-scale recirculation region is present downstream of the nozzle. As the nozzle remained open during the tests without plume, the recirculation region likely extends to inside the model. At the junction of the base and afterbody at  $x/D = 0$ , the majority of cases show evidence of a small secondary recirculation region, formed due to separation of the back flow over the afterbody.

Focussing on  $M_\infty = 0.76$ , it can be observed that for increasing nozzle lengths, the reattachment length does not significantly change, but the maximum backflow velocity decreases. For the two shortest nozzle lengths ( $L/D = 0.6$  and  $0.9$ ) the mean reattachment of the shear layer does not occur on the afterbody. If no plume is present, this leads to a merging of the recirculation regions downstream of the base and downstream of the afterbody. If a plume is present, the shear layer impinges on the plume. The two cases with the longer nozzle lengths ( $L/D = 1.2$  and  $1.8$ ), appear remarkably similar up to  $x \approx D$ , where mean reattachment occurs on the afterbody, regardless of the presence of a plume further downstream. Downstream of reattachment, the flow looks distinctly different however. For the longest nozzle length ( $L/D = 1.8$ ), the flow has the opportunity to recover after reattachment resulting in greater

streamwise velocity of the flow over the afterbody and further downstream. In absence of the plume, the case exhibits a more pronounced recirculation region downstream of the afterbody.

The comparison between  $M_\infty = 0.76$  and  $M_\infty = 2.20$  shows that the supersonic flow cases exhibit a greater deflection of the outer flow and a smaller recirculation region. In contrast to  $M_\infty = 0.76$ , reattachment occurs further downstream for longer nozzles, while the maximum backflow velocity increases. For the cases without plume, only for the shortest nozzle ( $L/D = 0.6$ ), reattachment does not occur on the afterbody. This case shows a small separation region on the afterbody at  $x/D = 0.5$  that is caused by separation of backflow over the trailing edge of the nozzle. For the cases with the plume, reattachment occurs on the plume for the two shortest nozzle lengths ( $L/D = 0.6$  and  $0.9$ ) and on the afterbody for the two longer nozzle lengths ( $L/D = 1.2$  and  $1.8$ ). The presence of the plume seems to slightly elongate the reattachment length.

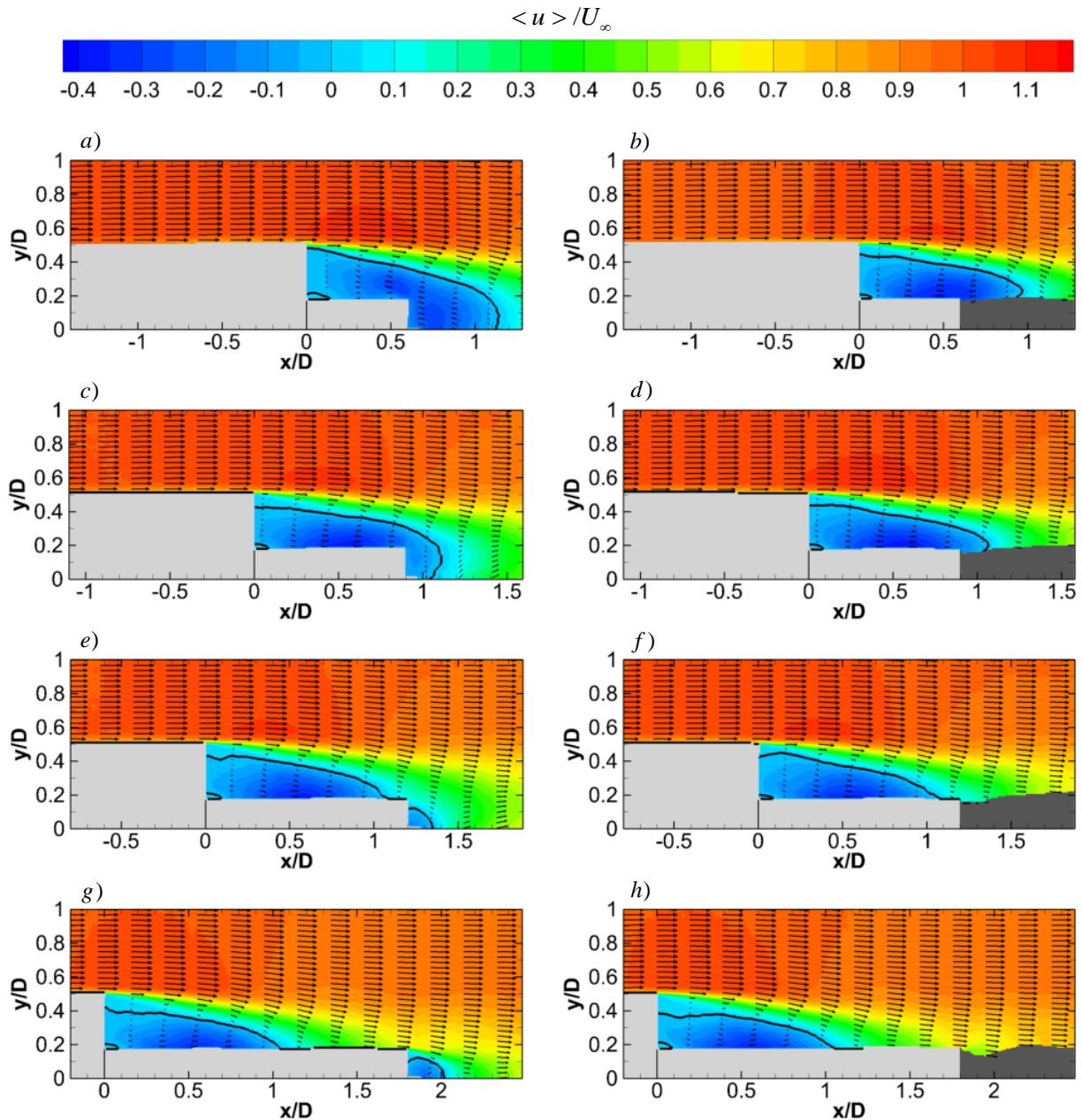
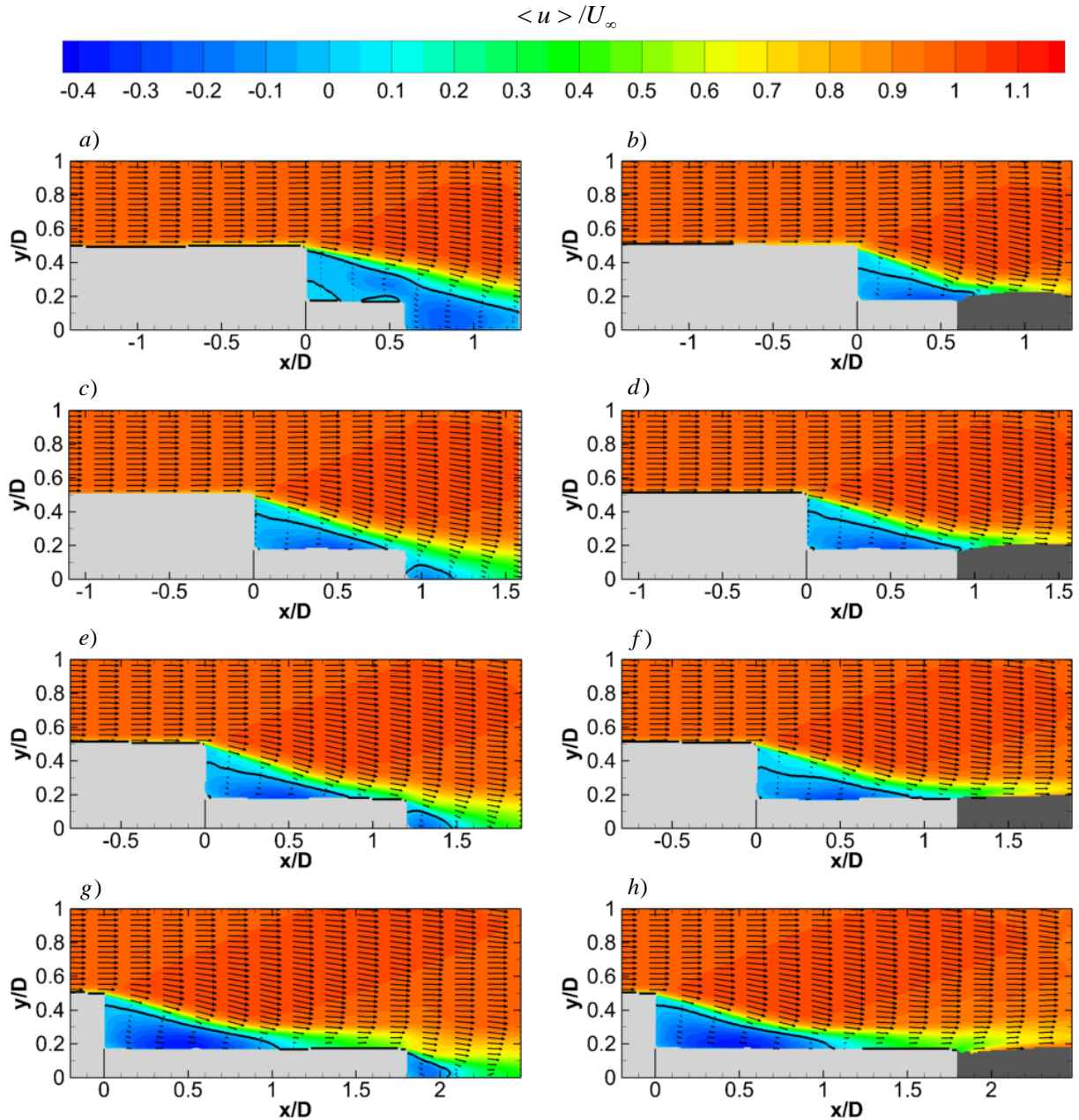


Figure 3: Mean streamwise velocity for  $M_\infty = 0.76$  for increasing nozzle lengths (top to bottom); no plume (left) and with plume (right); Solid black line indicates zero streamwise velocity

Table 2: Mean reattachment length ( $L_R$ ) and absolute value of maximum mean backflow velocity in the recirculation region over the afterbody ( $|\bar{u}_{\min}|$ )

	$M_\infty = 0.76$ (no plume)		$M_\infty = 0.76$ (plume)		$M_\infty = 2.20$ (no plume)		$M_\infty = 2.20$ (plume)	
	$L_R/D$	$ \bar{u}_{\min} /U_\infty$	$L_R/D$	$ \bar{u}_{\min} /U_\infty$	$L_R/D$	$ \bar{u}_{\min} /U_\infty$	$L_R/D$	$ \bar{u}_{\min} /U_\infty$
$L/D = 0.6$	n.a.	n.a.	0.9	0.40	n.a.	n.a.	0.6	0.28
$L/D = 0.9$	n.a.	n.a.	1.0	0.42	0.8	0.27	0.9	0.28
$L/D = 1.2$	1.1	0.39	1.1	0.38	0.9	0.31	1.0	0.29
$L/D = 1.8$	1.1	0.36	1.1	0.37	1.1	0.39	1.1	0.39

Figure 4: Mean streamwise velocity for  $M_\infty = 2.20$  for increasing nozzle lengths (top to bottom); no plume (left) and with plume (right); Solid black line indicates zero streamwise velocity

To assess the inflow conditions, Figure 5 shows the mean streamwise velocity over the model just upstream of the step, at  $x = -0.1D$ . Due to limitations in spatial resolution and practical difficulties to view close to the model surface, only the upper region of the boundary layer over the main body could be captured. Note that the freestream velocity used in the scaling is calculated from the measured total temperature ( $T_0$ ), the total pressure ( $p_0$ ) and the local static pressure ( $p_\infty$ ), using isentropic flow relations. The figures show little variation in inflow velocity between different cases. In general, the inflow velocity varies no more than  $0.01U_\infty$  between corresponding cases with and without plume (with the exception of  $L/D = 0.6$  at  $M_\infty = 0.76$ ) and by no more than  $0.04U_\infty$  between cases with different nozzle lengths.

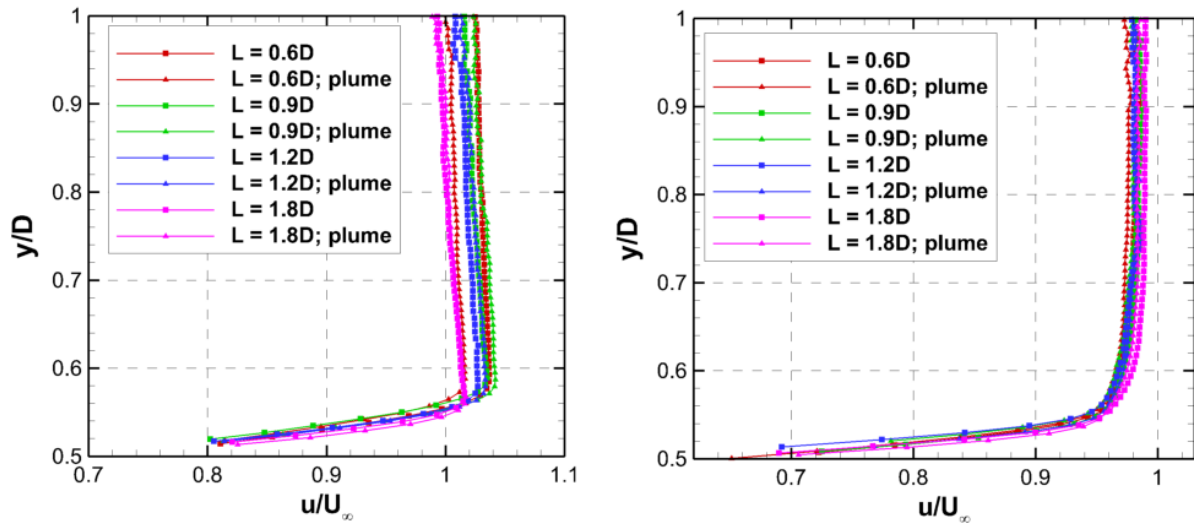


Figure 5: Mean streamwise velocity at  $x = -0.1D$  for  $M_\infty = 0.76$  (left) and  $M_\infty = 2.20$  (right)

### 3.2 Turbulent kinetic energy

To assess the unsteadiness of the flow, the turbulent kinetic energy (TKE) is estimated according to:  $TKE = (\langle (u')^2 \rangle + \langle (v')^2 \rangle) / 2$ . Figure 6 and Figure 7 show the organisation of the TKE for  $M_\infty = 0.76$  and  $M_\infty = 2.20$ , respectively. Note the difference in scale between both figures. Table 3 lists the maximum TKE levels in the shear layer to facilitate the comparison of the different flow cases. It should be noted that the flow contains structures with length scales that are similar or smaller than the spatial resolution of the PIV measurement. The PIV processing leads to modulation of the measured velocity distributions of such relatively small structures and therefore underestimation of TKE levels. This effect is especially pronounced in the shear layer close to the base which predominantly contains small flow structures.

In general, the figures show low levels of TKE in the outer flow and elevated levels in the shear layer and reattachment region. Typical TKE levels in the freestream corresponding to turbulence intensity levels in the range 1-2%  $U_\infty$ . More accurate hot-wire anemometry measurements performed at a freestream Mach number of 1.7 found a turbulence intensity of approximately 0.5%  $U_\infty$  (based on [35]). Elevated TKE levels in the top of the domain are attributed to higher measurement errors resulting from poorer flow seeding conditions. Propagation of these errors to the pressure calculation has been avoided by adjusting the fluctuation levels in the region  $y/D > 0.75$  to typical levels in the freestream, before the pressure reconstruction. The elevated levels in the shear layer and reattachment region can be attributed to the presence of small-scale structures in the instantaneous flow organisation as well as the unsteadiness of the flow, which is known to encompass flapping of the shear layer, vortex shedding and pulsing of the separated region [4].

For  $M_\infty = 0.76$ , the presence of the plume does not seem to greatly affect the organisation of TKE or the maximum TKE levels, except for the shortest nozzle length ( $L/D = 0.6$ ). Larger differences exist between flow cases with different nozzle lengths. The greatest TKE levels occur for  $L/D = 0.9$  and  $1.2$  for which the reattachment length ( $L_R$ ) is close to the afterbody length ( $L$ ) (compare Table 2). This increased unsteadiness for those flow cases may result from the intermittent occurrence of reattachment on the afterbody and the downstream flow (hybrid reattachment). In contrast, for the shortest nozzle length ( $L/D = 0.6$ ), reattachment always occurs on the downstream flow (fluidic reattachment) while for the longest nozzle length ( $L/D = 1.8$ ) reattachment always occurs on the afterbody (solid reattachment). Evidently, the latter situation results in the lowest TKE levels.

Compared to the subsonic flow cases, the supersonic flow cases at  $M_\infty = 2.20$  exhibit much smaller TKE levels relative to the squared freestream velocity ( $U_\infty^2$ ). Further, the regions of highest turbulence intensity occur closer to the afterbody. The flow cases with the three shortest nozzle lengths ( $L/D = 0.6, 0.9$  and  $1.2$ ) have similar maximum TKE levels, whereas the TKE levels for the longest nozzle length ( $L/D = 1.8$ ) are about twice as high. For the longest nozzle length however, the TKE levels are about twice as high. In the presence of a plume, the region with elevated TKE levels extends farther in streamwise direction.

Comparisons of flow cases with a long nozzle without plume and flow cases with a short nozzle but with a plume suggests that the presence of the plume cannot accurately be modelled by replacing the plume with a solid geometry.

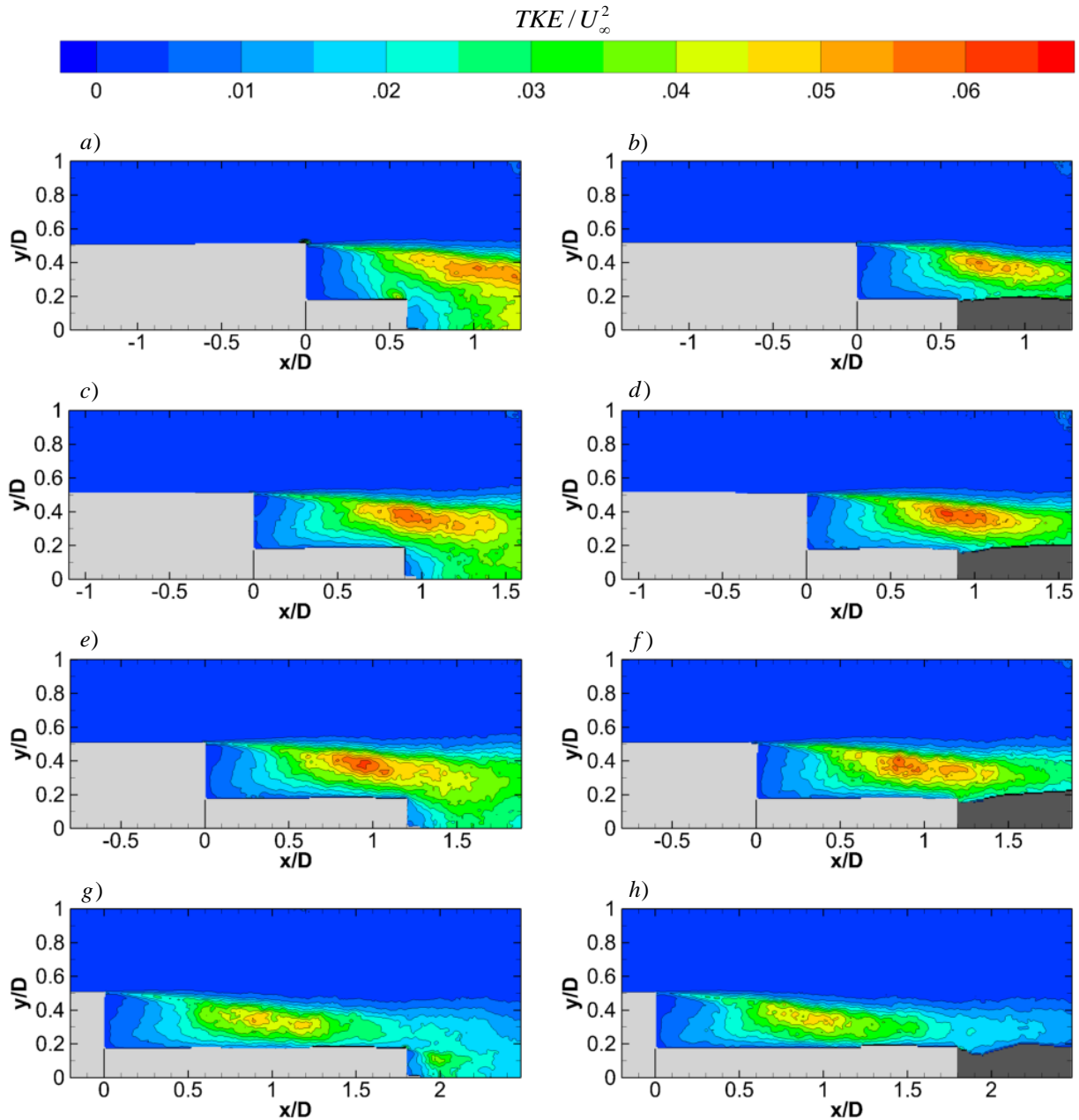
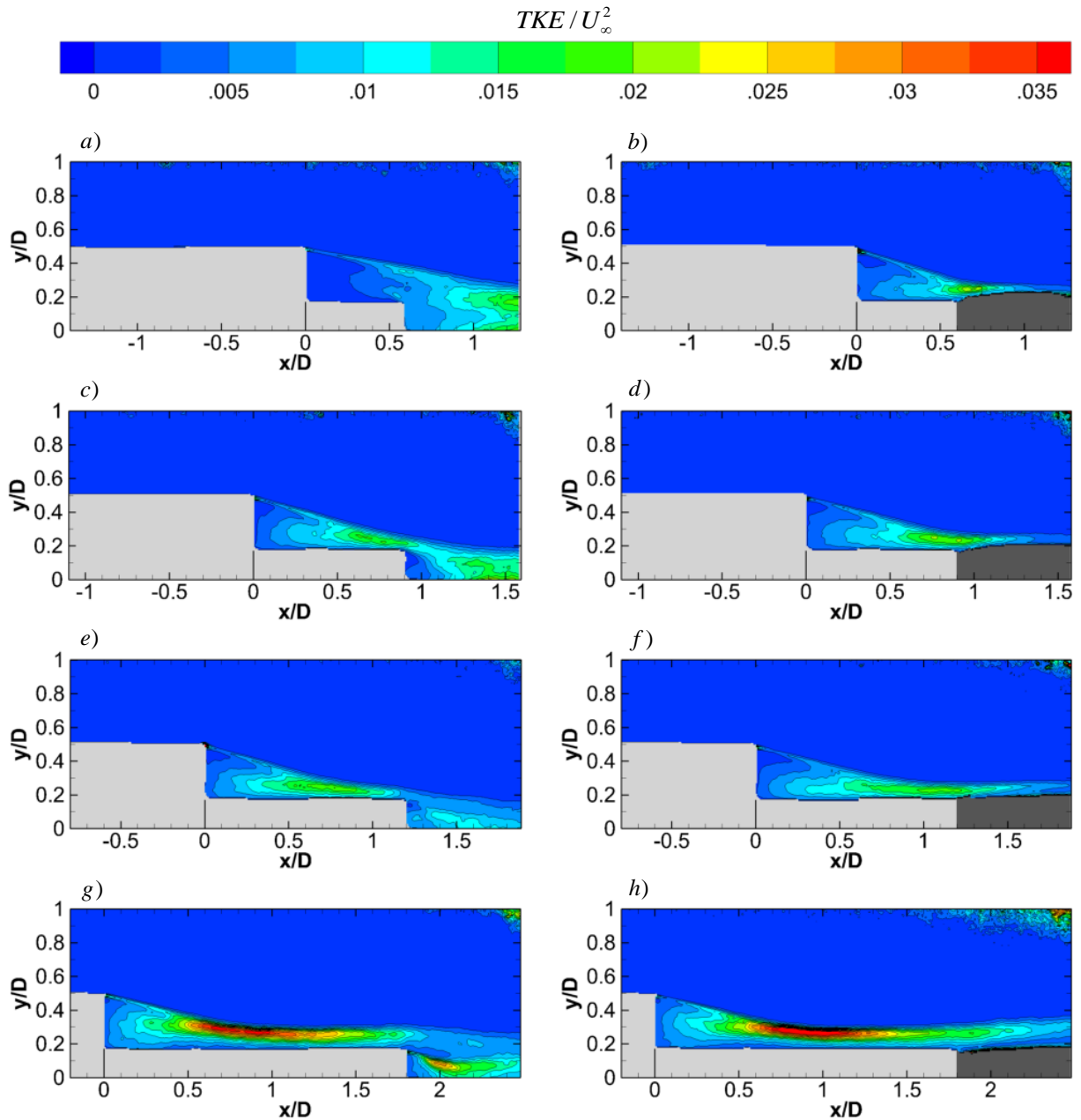


Figure 6: Turbulent kinetic energy for  $M_\infty = 0.76$  for increasing nozzle lengths (top to bottom); no plume (left) and with plume (right).

Table 3: Maximum turbulent kinetic energy (TKE) in the shear layer

	$M_\infty = 0.76$ (no plume) TKE / $U_\infty^2$	$M_\infty = 0.76$ (plume) TKE / $U_\infty^2$	$M_\infty = 2.20$ (no plume) TKE / $U_\infty^2$	$M_\infty = 2.20$ (plume) TKE / $U_\infty^2$
$L/D = 0.6$	.056	.058	.018	.022
$L/D = 0.9$	.060	.064	.018	.021
$L/D = 1.2$	.062	.061	.020	.019
$L/D = 1.8$	.051	.049	.038	.042

Figure 7: Turbulent kinetic energy for  $M_\infty = 2.20$  for increasing nozzle lengths (top to bottom); no plume (left) and with plume (right).

### 3.3 Mean pressure

Figure 8 and Figure 9 show the organisation of the mean pressure field for  $M_\infty = 0.76$  and  $M_\infty = 2.20$ , respectively. All pressure results are normalised according to  $C_p = 2(p-p_\infty)/(p_\infty\gamma M_\infty^2)$ . Comparison of the exact pressure levels is hampered by a systematic uncertainty in the overall pressure level for each case that is introduced by uncertainty of the boundary condition used during pressure reconstruction. The discussion therefore focusses on the relative distributions.

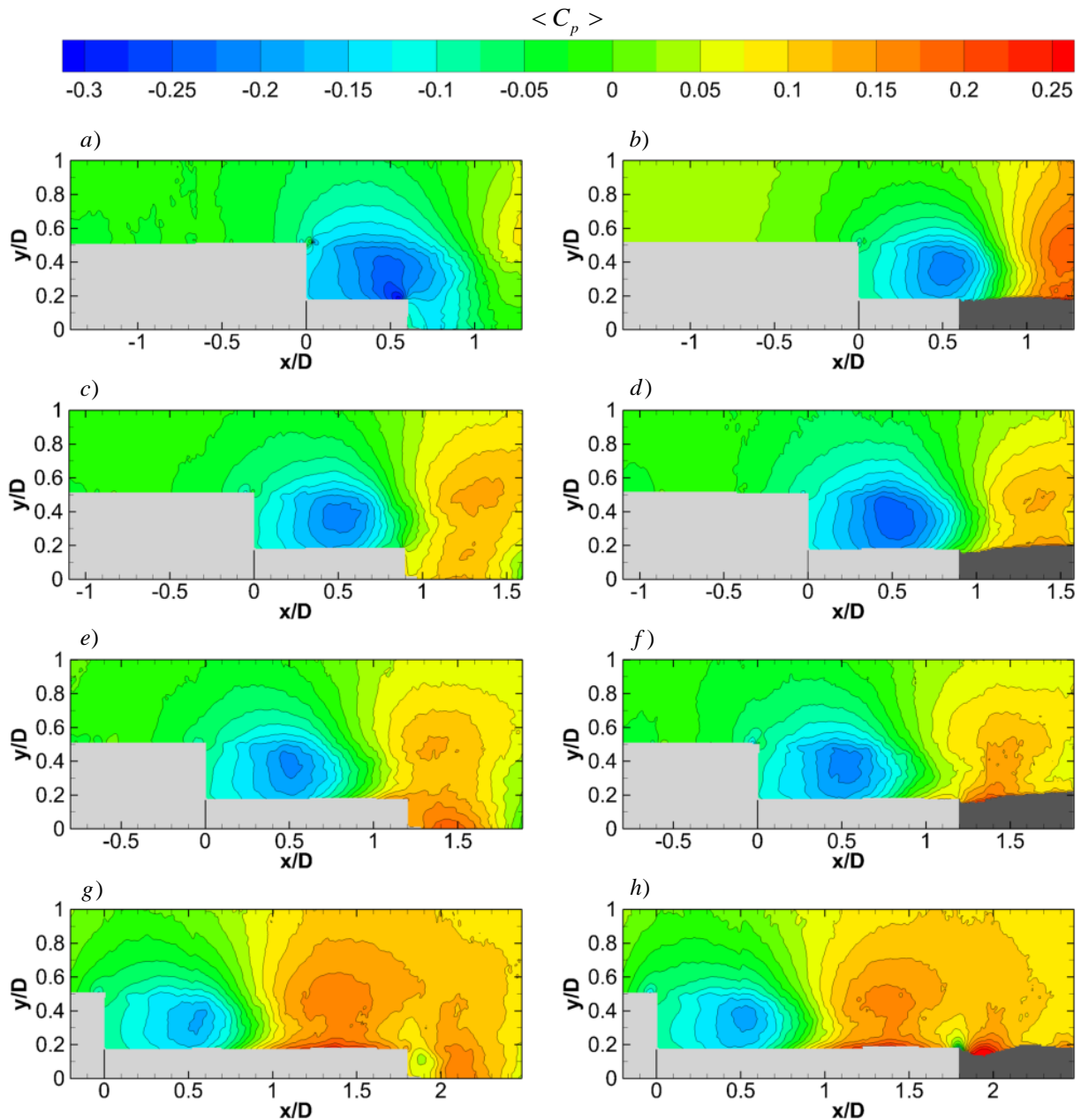


Figure 8: Mean pressure for  $M_\infty = 0.76$  for increasing nozzle lengths (top to bottom); no plume (left) and with plume (right).

In general, the figures show a low pressure region downstream of the base. The centre of this region is located at the centre of the recirculation region where the velocity is zero (compare Figure 3 and Figure 4). Downstream of the low pressure region, a high pressure region is present. Strong pressure gradients exist between the high and low pressure region. The bottom figures show that downstream of the location of maximum pressure, the pressure decreases again. Large differences exist between pressure fields for the subsonic and supersonic flow

cases. For  $M_\infty = 0.76$ , the low pressure region can be seen to extend upstream of the step. The supersonic cases show more oblique organisations of the pressure fields and higher pressure gradients due to the presence of an expansion fan at the step and shock waves at reattachment. Comparison of the flow cases with and without plume and for different nozzle lengths leads to a number of interesting observations. Firstly, the location of the low pressure region downstream of the base remains rather fixed for different flow cases. Secondly, as the nozzle length increases, the nozzle extends into the high pressure region. The plume is therefore introduced in a flow region with higher pressure, resulting in a less under-expanded or more over-expanded plume. The differences in the state of the plume were confirmed by means of Schlieren visualisation.

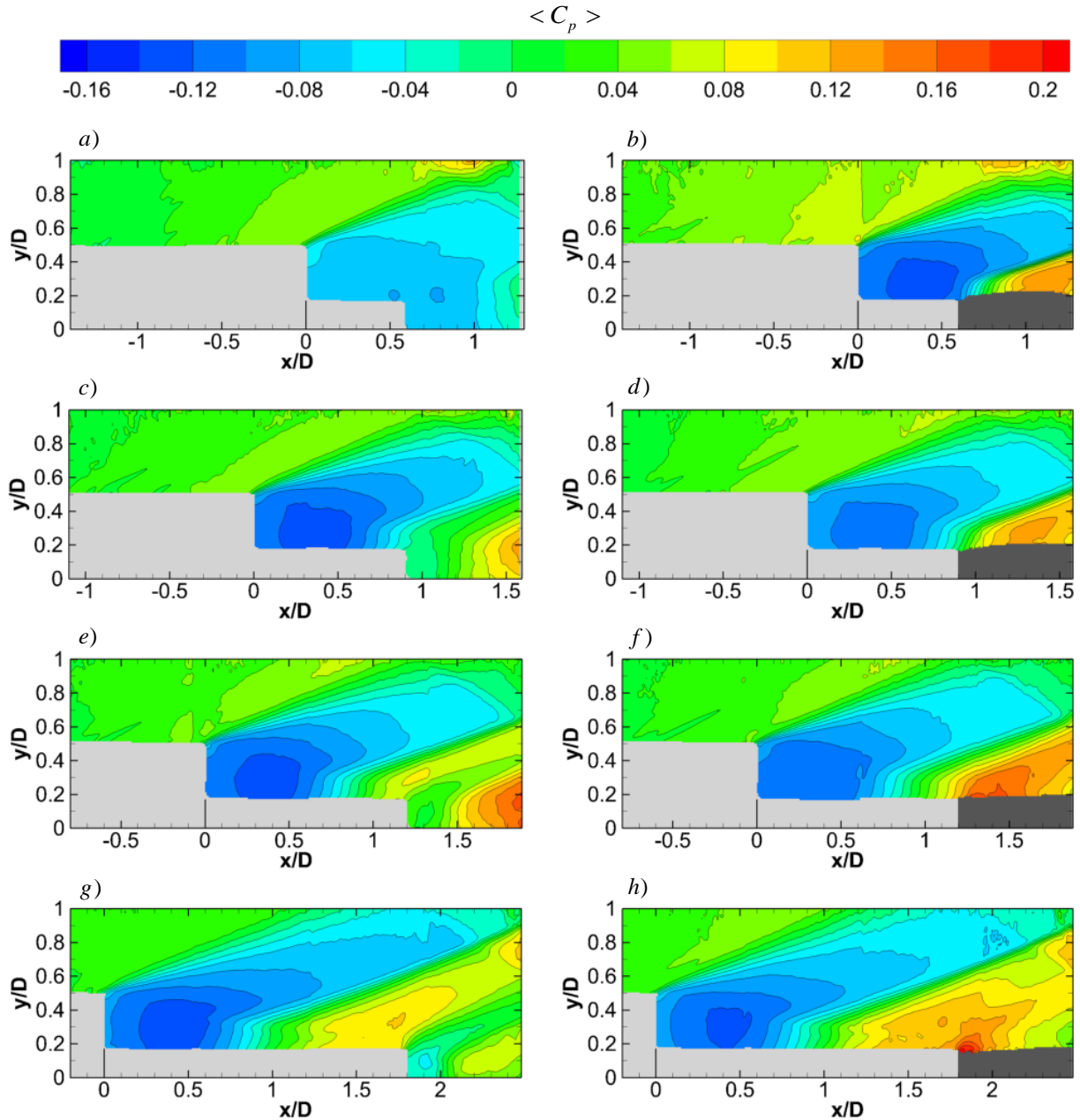


Figure 9: Mean pressure for  $M_\infty = 2.20$  for increasing nozzle lengths (top to bottom); no plume (left) and with plume (right).

### 3. Conclusions

PIV measurements have been carried out to study the effect of exhaust plume and nozzle length on the flow topology and mean pressure distribution of axisymmetric base flows at freestream Mach numbers 0.76 and 2.20. Four different nozzle lengths ( $L/D = 0.6, 0.9, 1.2, 1.8$ ) with and without exhaust plume have been tested. The use of different nozzle lengths resulted in flow cases in which the shear layer impinged on the model (solid reattachment), on the flow downstream of the model (fluidic reattachment), or intermittently on the model and on the flow (hybrid reattachment). Table 4 provides an overview of the comparison of different flow cases.

Table 4: Overview of comparison of flow cases

	$M_\infty = 0.76$	$M_\infty = 2.20$
Longer nozzles	No change in reattachment length Increase in maximum backflow velocity Strong decrease in TKE for solid reattachment	Increase in reattachment length Decrease in maximum backflow velocity Strong increase in TKE for solid reattachment
Impact of plume	No change in reattachment length	Increase in reattachment length Longer region with elevated TKE levels

For  $M_\infty = 0.76$ , neither an increase in nozzle length nor the presence of an exhaust plume was found to lead to a significant change in the mean reattachment length. For longer nozzles, the absolute maximum backflow velocity was however found to decrease. The relative turbulent kinetic energy ( $TKE/U_\infty^2$ ) for the flow case with solid reattachment was significantly lower than for the other subsonic flow cases.

For  $M_\infty = 2.20$ , both an increase in nozzle length and the presence of an exhaust plume were accompanied by a longer reattachment length. Contrary to the observed trends for the subsonic flow cases, for longer nozzles, the maximum backflow velocity was found to increase. Relative TKE levels for the flow case with solid reattachment were significantly higher than for the other supersonic flow cases. In addition, the presence of the plume led to an elongation of the region with elevated TKE levels.

Comparisons of flow cases with a long nozzle without a plume and flow cases with a short nozzle but with a plume suggest that the presence of the plume cannot accurately be modelled by replacing the plume with a solid geometry.

Mean pressure results showed large differences between the pressure fields for subsonic and supersonic flow cases. The location of the low-pressure region downstream of the base was observed to remain rather constant for different flow cases with and without plume and for different nozzle lengths. An increase in nozzle length was found to lead to a higher local pressure at the nozzle exit resulting in a less under-expanded or more over-expanded plume.

### Acknowledgements

This work has been supported by the European FP-7 project “NIOPLEX”, grant agreement 605151.

### References

- Schrijer, F.F.J., Sciacchitano, A., Scarano, F., Hannemann, K., Pallegoix, J.F., Maseland, J.E.J., Schwane, R.: Experimental Investigation of Base Flow Buffeting on the Ariane 5 Launcher Using High Speed PIV. 7th Eur. Symp. Aerothermodyn. 7, 1689–1699 (2011).
- Driver, D.M., Seegmiller, H.L., Marvin, J.G.: Time-dependent behaviour of a reattaching shear layer. Aiaa J. 25, 914–919 (1987).
- Loth, E., Kailasanath, K., Loehner, R.: Supersonic flow over an axisymmetric backward-facing step. J. Spacecr. Rockets. 29, 352–359 (1992).
- Deprés, D., Reijasse, P., Dussauge, J.P.: Analysis of Unsteadiness in Afterbody Transonic Flows. AIAA J. 42, 2541–2550 (2004).
- Bergman, D.: Effects of engine exhaust flow on boattail drag. 8th Aerosp. Sci. Meet. 8, 434–439 (1970).
- Statnikov, V., Sayadi, T., Meinke, M., Schmid, P., Schröder, W.: Analysis of pressure perturbation sources

- on a generic space launcher after-body in supersonic flow using zonal turbulence modeling and dynamic mode decomposition. *Phys. Fluids*. 27, (2015).
7. Weiss, P.-E., Deck, S., Robinet, J.-C., Sagaut, P.: On the dynamics of axisymmetric turbulent separating/reattaching flows. *Phys. Fluids*. 21, 75103 (2009).
  8. Hannemann, K., Lüdeke, H., Pallegoix, J., Ollivier, A., Lambaré, H., Maseland, J.E.J., Geurts, E., Frey, M., Deck, S., Schrijer, F., Scarano, F., Schwane, R.: Launch Vehicle Base Buffeting-Recent Experimental and Numerical Investigations. 7th European Symposium on Aerothermodynamics for Space Vehicles. , Brugge, Belgium (2011).
  9. Scharnowski, S., Statnikov, V., Meinke, M., Schröder, W., Kähler, C.J.: Combined experimental and numerical investigation of a transonic space launcher wake. In: Knight, D., Lipatov, I., and Reijasse, P. (eds.) *Progress in Flight Physics – Volume 7*. pp. 311–328. EDP Sciences, Les Ulis, France (2015).
  10. Schrijer, F.F.J., Sciacchitano, A., Scarano, F.: Spatio-temporal and modal analysis of unsteady fluctuations in a high-subsonic base flow. *Phys. Fluids*. 26, 86101 (2014).
  11. Deck, S., Simon, F., Merlen, A., Guillen, P., Sagaut, P.: Numerical simulation of the compressible mixing layer past an axisymmetric trailing edge. *J. Fluid Mech.* 591, 215–253 (2007).
  12. Janssen, J.R., Dutton, J.C.: Time-Series Analysis of Supersonic Base-Pressure Fluctuations. *AIAA J.* 42, 605–613 (2004).
  13. Scarano, F., van Oudheusden, B.W., Bannink, W.J., Bsibsi, M.: Experimental Investigation of Supersonic Base Flow Plume Interaction by Means of Particle Image Velocimetry. In: Danesy, D. (ed.) *Fifth European Symposium on Aerothermodynamics for Space Vehicles*. p. 601 (2005).
  14. Statnikov, V., Stephan, S., Pausch, K., Meinke, M., Radespiel, R., Schröder, W.: Experimental and numerical investigations of the turbulent wake flow of a generic space launcher at  $M_\infty = 3$  and  $M_\infty = 6$ . *CEAS Sp. J.* 8, 101–116 (2016).
  15. Bitter, M., Scharnowski, S., Hain, R., Kähler, C.J.: High-repetition-rate PIV investigations on a generic rocket model in sub- and supersonic flows. *Exp. Fluids*. 50, 1019–1030 (2011).
  16. Bolgar, I., Scharnowski, S., Kähler, C.J.: Investigation of a generic space launcher wake in sub-, trans- and supersonic conditions. *Sonderforschungsbereich/Transregio 40 – Annu. Rep.* 2016. 121–130 (2016).
  17. Statnikov, V., Glatzer, C., Meiß, J.-H., Meinke, M., Schröder, W.: Numerical investigation of the near wake of generic space launcher systems at transonic and supersonic flows. In: Reijasse, P., Knight, D., Ivanov, M., and Lipatov, I. (eds.) *Progress in Flight Physics*. pp. 191–208. EDP Sciences, Les Ulis, France (2013).
  18. Scharnowski, S., Kähler, C.J.: Investigation of a transonic separating/reattaching shear layer by means of PIV. *Theor. Appl. Mech. Lett.* 5, 30–34 (2015).
  19. Scharnowski, S., Bolgar, I., Kähler, C.J.: Control of the Recirculation Region of a Transonic Backward-Facing Step Flow Using Circular Lobes. *International Symposium on Turbulence and Shear Flow Phenomena (TSGP-9)*. pp. 1–6. , Melbourne, Australia (2015).
  20. Schrijer, F.F.J., Sciacchitano, A., Scarano, F.: Experimental investigation of flow control devices for the reduction of transonic buffeting on rocket afterbodies. 5–8 (2010).
  21. Blinde, P., Lynch, K., Oudheusden, B. van, Schneiders, J., Schrijer, F.: Assessment of instantaneous pressure determination in a transonic base flow based on four-pulse tomographic PIV. *17th International Symposium on Applications of Laser Techniques to Fluid Mechanics*. , Lisbon, Portugal (2014).
  22. van Gent, P.L., Michaelis, D., van Oudheusden, B.W., Weiss, P.-É., de Kat, R., Laskari, A., Jeon, Y.J., David, L., Schanz, D., Huhn, F., Gesemann, S., Novara, M., McPhaden, C., Neeteson, N.J., Rival, D.E., Schneiders, J.F.G., Schrijer, F.F.J.: Comparative assessment of pressure field reconstructions from particle image velocimetry measurements and Lagrangian particle tracking. *Exp. Fluids*. 58, 33 (2017).
  23. van Oudheusden, B.W.: PIV-based pressure measurement. *Meas. Sci. Technol.* 24, 32001 (2013).
  24. Hirschel, E.: Vehicle Design and Critical Issues; FESTIP Technology Development Work in Aerothermodynamics for Reusable Launch Vehicles. *ESA/ESTEC FESTIP Workshop*. , Noordwijk (1996).
  25. Bakker, P., Bannink, W., Serval, P., Reijasse, P.: CFD validation for base flows with and without plume interaction. *40th AIAA Aerosp. Sci. Meet. Exhib.* (2002).
  26. Bannink, W., Houtman, E., Bakker, P.: Base flow/underexpanded exhaust plume interaction in a supersonic external flow. *8th AIAA International Space Planes and Hypersonic Systems and Technologies Conference*. American Institute of Aeronautics and Astronautics, Reston, Virginia (1998).
  27. Ariane Space: Ariane 5 User's Manual. Ariane Space (2016).
  28. SpaceFlight101.com: Ariane 5 - VA226 - Launch Profile, <http://spaceflight101.com/ariane-5-va226/ariane-5-va226-launch-profile/>.
  29. Pindzola, M.: Jet simulation in ground test facilities. North Atlantic Treaty Organization, Advisory Group for Aeronautical Research and Development, [Paris] (1963).
  30. Schrijer, F.F.J., Scarano, F., van Oudheusden, B.W.: Application of PIV in a Mach 7 double-ramp flow. *Exp. Fluids*. 41, 353–363 (2006).

31. Ragni, D., Schrijer, F., van Oudheusden, B.W., Scarano, F.: Particle tracer response across shocks measured by PIV. *Exp. Fluids*. 50, 53–64 (2010).
32. van Oudheusden, B.W.: Principles and application of velocimetry-based planar pressure imaging in compressible flows with shocks. *Exp. Fluids*. 45, 657–674 (2008).
33. van Oudheusden, B.W., Scarano, F., Roosenboom, E.W.M., Casimiri, E.W.F., Souverein, L.J.: Evaluation of integral forces and pressure fields from planar velocimetry data for incompressible and compressible flows. *Exp. Fluids*. 43, 153–162 (2007).
34. Jeon, Y.J., Chatellier, L., Beaudoin, A., Laurent, D.: Least-square reconstruction of instantaneous pressure field around a body based on a directly acquired material acceleration in time-resolved PIV. 11th International Symposium on Particle Image Velocimetry - PIV15. , Santa Barbara, CA (2015).
35. Giepmans, R.H.M., Schrijer, F.F.J., van Oudheusden, B.W.: High-resolution PIV measurements of a transitional shock wave–boundary layer interaction. *Exp. Fluids*. 56, 113 (2015).